






The JPL Planetary and Lunar Ephemerides DE440 and DE441

Ryan S. Park , William M. Folkner , James G. Williams , and Dale H. BoggsJet Propulsion Laboratory, California Institute of Technology, 4800 Oak Grove Drive, Pasadena, CA 91109-8099, USA; Ryan.S.Park@jpl.nasa.gov

Received 2020 November 11; revised 2020 December 8; accepted 2020 December 15; published 2021 February 8

Abstract

The planetary and lunar ephemerides called DE440 and DE441 have been generated by fitting numerically integrated orbits to ground-based and space-based observations. Compared to the previous general-purpose ephemerides DE430, seven years of new data have been added to compute DE440 and DE441, with improved dynamical models and data calibration. The orbit of Jupiter has improved substantially by fitting to the Juno radio range and Very Long Baseline Array (VLBA) data of the Juno spacecraft. The orbit of Saturn has been improved by radio range and VLBA data of the Cassini spacecraft, with improved estimation of the spacecraft orbit. The orbit of Pluto has been improved from use of stellar occultation data reduced against the Gaia star catalog. The ephemerides DE440 and DE441 are fit to the same data set, but DE441 assumes no damping between the lunar liquid core and the solid mantle, which avoids a divergence when integrated backward in time. Therefore, DE441 is less accurate than DE440 for the current century, but covers a much longer duration of years $-13,200$ to $+17,191$, compared to DE440 covering years 1550–2650.

Unified Astronomy Thesaurus concepts: [Celestial mechanics \(211\)](#); [Orbital motion \(1179\)](#); [Orbits \(1184\)](#); [Solar system planets \(1260\)](#); [Solar system \(1528\)](#); [The Sun \(1693\)](#); [The Moon \(1692\)](#); [Earth-moon system \(436\)](#); [Solar system astronomy \(1529\)](#); [Pluto \(1267\)](#)

1. Introduction

Modern-day planetary ephemerides are computed by fitting numerically integrated orbits to various types of ground-based and space-based observations (Folkner et al. 2014; Pitjeva & Pitjev 2018; Fienga et al. 2020). The Jet Propulsion Laboratory’s (JPL) planetary and lunar ephemerides Development Ephemeris (DE) series includes the positions of the Sun, the barycenters of eight planetary systems, the Moon, the Pluto system barycenter, and lunar libration angles, as well as their associated velocities. The high-precision orbits and lunar rotations around the three axes have a wide range of practical and fundamental applications (Thornton & Border 2003; Park et al. 2020b; Vallisneri et al. 2020; U.S. Nautical Almanac Office & Her Majesty’s Nautical Almanac Office 2018). Without an update, however, the errors in orbits grow for several reasons. For Jupiter (Juno 2016–2020 < 12 yr period), Saturn (Cassini 2004–2018, < 30 yr period), Uranus, Neptune, and Pluto the high-quality data are available for less than one orbit. For Mars, the range data is of high quality, but the main-belt asteroid masses are a limitation partly due to the large number of asteroids and partly due to long-period perturbations (Folkner et al. 2014). In the future, these errors grow nonlinearly with time.

The planetary and lunar ephemerides DE440 replaces DE430 released in 2014 (Folkner et al. 2014) and its precursors. Since the DE430 release, several interim ephemerides have been released. Each interim DE file was for a specific flight project, which has been tuned for the flight project’s target body. For example, the last release was DE438 in 2018 for the Juno mission (Bolton et al. 2017). DE440 has updated all bodies using all available data, including the Moon, which has not been updated since DE430.

Since DE430, several updates have been made to the dynamical model used to integrate DE440. Perturbations from 30 individual Kuiper belt objects (KBOs) and a circular ring representing the rest of the Kuiper belt, modeled as 36 point masses with an equal mass located at 44 au, have been added to the model (Pitjeva & Pitjev 2018). The Lense–Thirring (LT)

effect from the Sun’s angular momentum has also been added (Park et al. 2017). For the orientation of Earth, the Vondrak precession model has been used (Vondrak et al. 2011), which, according to Vondrak et al. (2009), is more accurate for integrations beyond ± 1000 years than the Lieske precession model (Lieske 1979) used for DE430. For the Moon, the effect of geodetic precession on lunar librations has been added as well as the solar radiation pressure force on the Earth–Moon system orbits.

Compared to DE430, new data spanning over about 7 years have been added to compute DE440. The shapes of Mercury, Venus, and Mars orbits are determined mainly by the radio range data of the MErcury Surface, Space ENvironment, GEOchemistry, and Ranging (MESSENGER), Venus Express, and Mars-orbiting spacecraft, respectively. The orientations of inner planet orbits are tied to the International Celestial Reference Frame (ICRF) via Very Long Baseline Interferometry (VLBI) of Mars-orbiting spacecraft (Folkner & Border 2015; Park et al. 2015). The orbit of the Moon is determined from laser ranging to lunar retroreflectors. The orbit accuracy of Jupiter has improved substantially by fitting the orbit to the radio range and Very Long Baseline Array (VLBA) data of the Juno spacecraft. The orbit of Saturn is determined by the radio range and VLBA data of the Cassini spacecraft, with improved spacecraft orbits used for processing the radio range data. The orbits of Uranus and Neptune are determined by astrometry and radio range measurements to the Voyager flybys. The orbit of Pluto is now mainly determined by stellar occultations reduced against the Gaia star catalog (Gaia Collaboration et al. 2018; Desmars et al. 2019).

For the Moon, viscous damping between the liquid core and the solid mantle are observed in the lunar laser ranging (LLR) data. This implies an excitation of the relative motion of a lunar core and mantle in the past, possibly due to a spin/orbit resonance that occurred in geologically recent times (Rambaux & Williams 2011). Both DE440 and DE441 have been fit to the same data set, but DE441 assumed no damping between the lunar liquid core and the solid mantle. In this way, a divergence



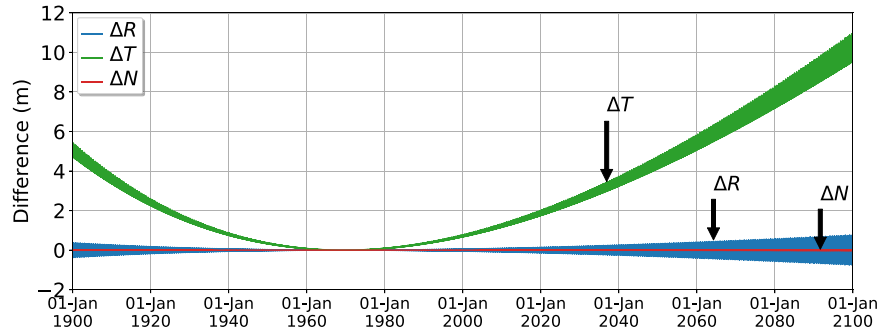


Figure 1. Difference in the lunar orbit relative to Earth between DE440 and DE441 (i.e., DE441 minus DE440) in radial (R), transverse (T), and normal (N) directions.

can be avoided when integrated backward for thousands of years. As a consequence, DE441 is less accurate than DE440 for the current century, but more accurate over longer past time spans. DE441 covers years $-13,200$ to $+17,191$, compared to DE440 covering years 1550 – 2650 . The difference in the orbits of the planets between DE440 and DE441 are less than 1 m over the 1100 years of the DE440 time span. The difference in the orbit of the Moon between DE440 and DE441 is less than 2 m during the time span of the LLR data, i.e., 1970 – 2020 , but increased over a longer time span, especially in the along-track direction (i.e., velocity direction). Figure 1 shows the difference in the lunar orbit relative to Earth between DE440 and DE441 over 200 years (i.e., DE441 minus DE440). In general, DE440 is recommended for analyzing modern data while DE441 is recommended for analyzing historical data earlier than the modern range data.

2. Coordinates of Planetary and Lunar Ephemerides

2.1. Inertial Reference Frame

The inertial coordinate frame of the planetary and lunar ephemerides is connected to the International Celestial Reference System (ICRS). The current ICRS realization is achieved by VLBI measurements of the positions of extragalactic radio sources (i.e., quasars) defined in the Third Realization of the International Celestial Reference Frame (ICRF3; Charlot et al. 2020), which is adopted by the International Astronomical Union (IAU). The orbits of the inner planets are tied to ICRF3 via VLBI measurements of Mars-orbiting spacecraft (Konopliv et al. 2016) with respect to quasars with positions known in the ICRF. Overall, the orientations of inner planet orbits are aligned with ICRF3 with an average accuracy of about 0.2 mas (Folkner & Border 2015; Folkner et al. 2014; Park et al. 2015). The orbits of Jupiter and Saturn are tied to ICRF3 via VLBA measurements of Juno and Cassini spacecraft (Jones et al. 2020), respectively.

2.2. Solar System Barycenter

The solar system barycenter (SSBC) is defined as (Estabrook 1971)

$$\mathbf{r}_{\text{ssbc}} = \left(\sum_i \mu_i^* \mathbf{r}_i \right) / \left(\sum_i \mu_i^* \right). \quad (1)$$

Here, the summation is over all bodies with finite mass, \mathbf{r}_i is the position of body i , and μ_i^* is defined as

$$\mu_i^* = GM_i \left(1 + \frac{1}{2c^2} v_i^2 - \frac{1}{2c^2} \sum_{j \neq i} \frac{GM_j}{r_{ij}} \right), \quad (2)$$

where GM_i is the mass parameter of body i , c is the speed of light, v_i is the barycentric speed of body i , and $r_{ij} = |\mathbf{r}_i - \mathbf{r}_j|$ is the distance between bodies i and j .

For DE440, the bodies used for computing the SSBC were the Sun, barycenters of eight planetary systems, the Pluto system barycenter, 343 asteroids, 30 KBOs, and a KBO ring representing the main Kuiper belt. The 343 asteroids were the same set of asteroids used in DE430, which consist of $\sim 90\%$ of the total asteroid-belt mass. The mass of the 30 largest known KBOs were from Pitjeva & Pitjev (2018). The circular KBO ring was modeled as 36 point masses with equal mass located in the ecliptic plane with a semimajor axis of 44 au, with the ring mass estimated.

Figure 2 shows the motion of the SSBC relative to the Sun for 100 years (2000 – 2100), which is sometimes called the solar inertial motion (SIM). Compared to DE430, SSBC has shifted by ~ 100 km, which is mainly due to the addition of KBOs. It is important to note that, to the first order, Earth orbits around the Sun, not around the SSBC. This point is reflected in Figure 3, which shows the time history of the closest (e.g., perihelion) and farthest (e.g., aphelion) points of the Earth–Moon barycenter (EMB) relative to the Sun and the SSBC. The near-constant distance of the perihelion and aphelion of the EMB relative to the Sun indicates that SIM does not affect the orbit of Earth relative to the Sun.

2.3. Ephemeris Coordinate Time

JPL’s DE series are integrated using the barycentric dynamical time (TDB), which is defined relative to the barycentric coordinate time (TCB; Petit & Luzum 2009). All of the data used to compute DE440 and DE441 had the intrinsic time tag in the coordinated universal time (UTC), which differs from the international atomic time (TAI) by leap seconds (i.e., $\text{TAI} = \text{UTC} + \text{leap seconds}$). In order to process these UTC-tagged measurements, the conversion from UTC to TDB would be needed (Soffel et al. 2003; Petit & Luzum 2009). Once the TAI time is computed, 32.184 s are added to compute the terrestrial time (TT; i.e., $\text{TT} = \text{TAI} + 32.184$ s). The

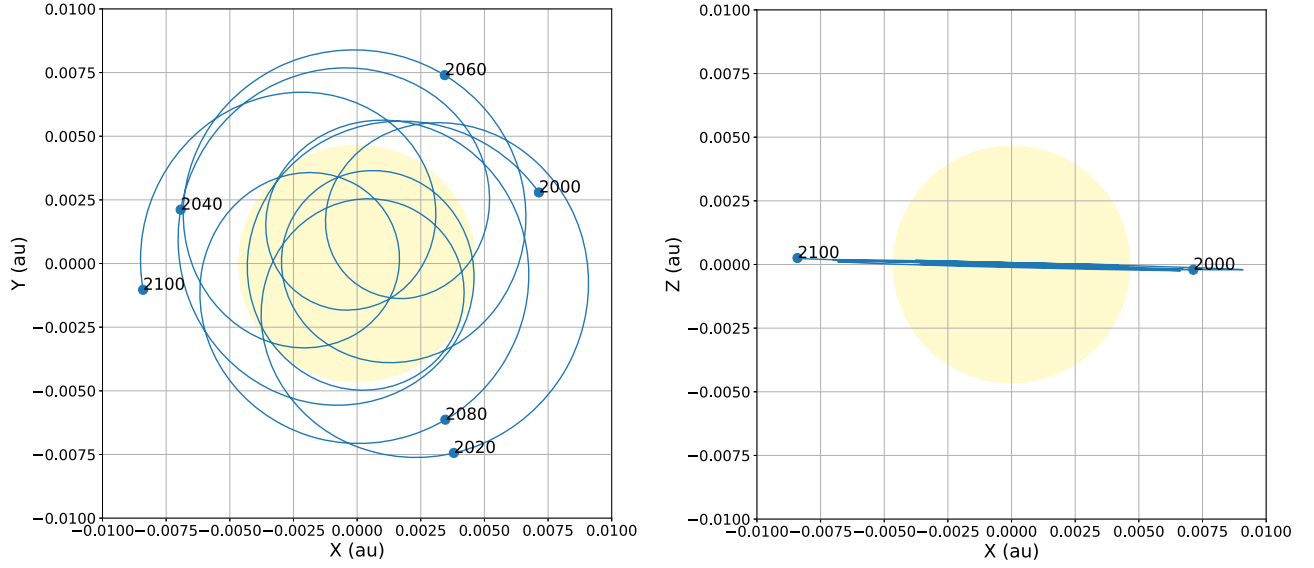


Figure 2. Position of the solar system barycenter relative to the Sun in XY (left) and XZ (right) heliocentric ecliptic planes, respectively. The yellow circle represents the Sun.

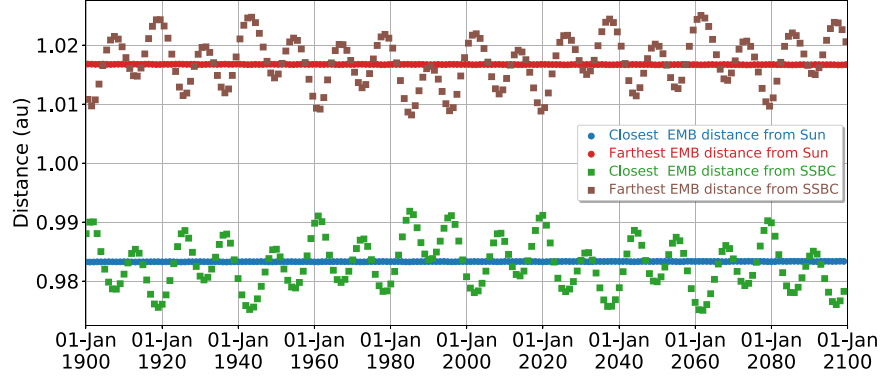


Figure 3. Distances of the closest and farthest points of the Earth–Moon barycenter relative to the Sun and SSBC of DE440.

conversion from TT to TDB (in Julian days) is given by

$$\begin{aligned}
 \text{TDB} - \text{TT} = & \frac{L_G - L_B}{1 - L_B} (\text{TDB} - T_0) + \frac{1 - L_G}{1 - L_B} \text{TDB}_0 \\
 & + \frac{1 - L_G}{1 - L_B} \int_{T_0 + \text{TDB}_0}^{\text{TDB}} \frac{1}{c^2} \left(\frac{v_E^2}{2} + w_{0E} + w_{LE} \right) dt \\
 & + \frac{1}{c^2} \mathbf{v}_E \cdot (\mathbf{r}_S - \mathbf{r}_E) \\
 & - \frac{1 - L_G}{1 - L_B} \int_{T_0 + \text{TDB}_0}^{\text{TDB}} \frac{1}{c^4} \left(-\frac{v_E^4}{8} - \frac{3}{2} v_E^2 w_{0E} \right. \\
 & \quad \left. + 4 \mathbf{v}_E \cdot \mathbf{w}_{iE} + \frac{1}{2} w_{0E}^2 + \Delta_E \right) dt \\
 & + \frac{1}{c^4} \left(3w_{0E} + \frac{v_E^2}{2} \right) \mathbf{v}_E \cdot (\mathbf{r}_S - \mathbf{r}_E),
 \end{aligned} \tag{3}$$

where $L_G = 6.969290134 \times 10^{-10}$ defines the rate of TT with respect to geocentric coordinate time (TCG), $L_B = 1.550519768 \times 10^{-8}$ defines the rate of TDB with respect to TCB, T_0 is

2443144.5003725 Julian days, $\text{TDB}_0 = -65.5 \times \frac{10^{-6}}{86400}$ days, v_E is the velocity of the Earth, \mathbf{v}_E is the velocity vector of the Earth, \mathbf{r}_E is the position vector of the Earth, and \mathbf{r}_S is the position vector of a measurement station. The potential term w_{0E} is defined as

$$w_{0E} = \sum_{i \neq E} \frac{GM_i}{r_{iE}}, \tag{4}$$

with the summation over all bodies other than Earth. The potential due to external oblate figures w_{LE} is defined as

$$w_{LE} = -\frac{GM_\odot J_{2\odot}}{|\mathbf{r}_\odot - \mathbf{r}_E|^3} \frac{R_\odot^2}{2} (3 \sin^2 \varphi_{E,\odot} - 1), \tag{5}$$

where $J_{2\odot}$ is the unnormalized second-degree gravitational zonal harmonic of the Sun, R_\odot is the solar radius, and $\varphi_{E,\odot}$ is the heliocentric ecliptic latitude of Earth. The term w_{iE} is defined as

$$w_{iE} = \sum_{i \neq E} \frac{GM_i v_i}{r_{iE}}, \tag{6}$$

where the summation is over all bodies other than Earth. Lastly, Δ_E is defined as

$$\Delta_E = \sum_{i \neq E} \frac{GM_i}{r_{iE}} \left[-2v_i^2 + \sum_{j \neq i} \frac{GM_j}{r_{ij}} + \frac{1}{2} \left(\frac{\mathbf{v}_i \cdot (\mathbf{r}_E - \mathbf{r}_i)}{r_{iE}} \right)^2 + \frac{1}{2} \mathbf{a}_i \cdot (\mathbf{r}_E - \mathbf{r}_i) \right], \quad (7)$$

where \mathbf{a}_i is the acceleration of body i and the summation is over all bodies.

2.4. Orientation of the Moon

LLR measures the round-trip light time of a laser pulse between an Earth LLR station and a retroreflector on the Moon. Thus, LLR data are not only sensitive to where the Moon is, but they are also sensitive to its orientation.

The orientation of lunar exterior (mantle and crust, hereafter referred to as the mantle) is defined by the principal axes (PAs) of the undistorted lunar mantle, and thus its moment of inertia matrix is diagonal. The directions of the PAs are taken from analyses of the Gravity Recovery and Interior Laboratory (GRAIL) data (Konopliv et al. 2013; Lemoine et al. 2013). The Euler angles that define the rotation from the PA frame to the inertial ICRF3 frame are: ϕ_m , the angle from the X-axis of the inertial frame along the XY plane to the intersection of the mantle equator; θ_m , the inclination of the mantle equator from the inertial XY plane; and ψ_m , the longitude from the intersection of the inertial XY plane with the mantle equator along the mantle equator to the prime meridian. The rotation from the lunar PA frame (i.e., lunar mantle frame) to ICRF3 is given as

$$\mathbf{r}_I = \mathcal{R}_z(-\phi_m) \mathcal{R}_x(-\theta_m) \mathcal{R}_z(-\psi_m) \mathbf{r}_{PA}. \quad (8)$$

The Euler angles ϕ_m , θ_m , and ψ_m are also known as lunar libration angles, stored in the DE440 and DE441 files. The rotation matrices use the right-hand rule and are defined as

$$\mathcal{R}_x(\alpha) = \begin{bmatrix} 1 & 0 & 0 \\ 0 & +\cos \alpha & +\sin \alpha \\ 0 & -\sin \alpha & +\cos \alpha \end{bmatrix}, \quad (9)$$

$$\mathcal{R}_y(\alpha) = \begin{bmatrix} +\cos \alpha & 0 & -\sin \alpha \\ 0 & 1 & 0 \\ +\sin \alpha & 0 & +\cos \alpha \end{bmatrix}, \quad (10)$$

$$\mathcal{R}_z(\alpha) = \begin{bmatrix} +\cos \alpha & +\sin \alpha & 0 \\ -\sin \alpha & +\cos \alpha & 0 \\ 0 & 0 & 1 \end{bmatrix}. \quad (11)$$

These lunar libration angles are integrated simultaneously with the orbital motion. The equations of motion for the lunar libration angles are

$$\dot{\phi}_m = (\omega_{m,x} \sin \psi_m + \omega_{m,y} \cos \psi_m) / \sin \theta_m, \quad (12)$$

$$\dot{\theta}_m = \omega_{m,x} \cos \psi_m - \omega_{m,y} \sin \psi_m, \quad (13)$$

$$\dot{\psi}_m = \omega_{m,z} - \dot{\phi}_m \cos \theta_m, \quad (14)$$

where $\omega_{m,x}$, $\omega_{m,y}$, and $\omega_{m,z}$ represent the components of the lunar mantle angular velocity $\boldsymbol{\omega}_m$ expressed in the mantle frame. The time derivatives of $\boldsymbol{\omega}_m$ are given in Section 4.

Table 1
XYZ Coordinates of Lunar Retroreflectors in the DE440 PA Frame and the DE421 MER Frame

Retroreflectors	DE440 PA Frame (m)	DE421 MER Frame (m)
Apollo 11	1591967.049	1591747.649
	690698.573	691222.200
	21004.461	20398.110
Apollo 14	1652689.369	1652818.682
	-520998.431	-520454.587
	-109729.869	-110361.165
Apollo 15	1554678.104	1554937.504
	98094.498	98604.886
	765005.863	764412.810
Lunokhod 2	1339363.598	1339388.213
	801870.995	802310.527
	756359.260	755849.393
Lunokhod 1	1114291.452	1114958.865
	-781299.273	-780934.127
	1076059.049	1075632.692

The lunar orientation model includes a fluid core. The orientation of the core with respect to the ICRF is represented by the Euler angles ϕ_c , θ_c , and ψ_c , which are also numerically integrated. Since the shape of the core/mantle boundary is modeled as fixed to the frame of the mantle, it is more convenient to express the core angular velocities with respect to the mantle frame. The time derivatives of the core Euler angles are then given by

$$\dot{\phi}_c = \omega_{c,z}^\dagger - \psi_c \cos \theta_c, \quad (15)$$

$$\dot{\theta}_c = \omega_{c,x}^\dagger, \quad (16)$$

$$\dot{\psi}_c = -\omega_{c,y}^\dagger / \sin \theta_c, \quad (17)$$

where the core angular velocity $\boldsymbol{\omega}_c$ is related to the angular velocity $\boldsymbol{\omega}_c^\dagger$ in a frame defined by the intersection of the core equator with the inertial XY plane by

$$\boldsymbol{\omega}_c^\dagger = \mathcal{R}_z(\phi_c - \phi_m) \mathcal{R}_x(-\theta_m) \mathcal{R}_z(-\psi_m) \boldsymbol{\omega}_c. \quad (18)$$

The time derivatives of $\boldsymbol{\omega}_c$ are given in Section 4.

Most of lunar cartographic products are defined relative to the DE421 mean-Earth/mean-rotation (MER) frame. The MER frame is defined by the X-axis pointing toward the mean-Earth direction and the Z-axis pointing toward the mean-rotation axis direction. The rotation from the DE440 PA frame to the DE421 MER frame is estimated by comparing the coordinates of the lunar retroreflectors estimated in the DE440 PA frame and the retroreflector coordinates in the DE421 MER frame, which yield

$$\mathbf{r}_{MER,DE421} = \mathcal{R}_x(-0''2785) \mathcal{R}_y(-78''6944) \times \mathcal{R}_z(-67''8526) \mathbf{r}_{PA,DE440}. \quad (19)$$

Table 1 shows the five lunar retroreflector positions in the DE440 PA frame and the corresponding lunar retroreflector positions in the DE421 MER frame.

2.5. Orientation of Earth

Only the long-term change of the Earth orientation is modeled in the ephemeris integration. The Earth orientation model used for DE440 and DE441 is based on a long-term precession model (Vondrak et al. 2011) and a modified

nutation model based on the IAU 1980 precession model including only terms with a period of 18.6 years.

The Earth pole unit vector in the inertial frame, \mathbf{p}_E , can be computed by the following steps.

First, the mean longitude of the ascending node of the lunar orbit measured on the ecliptic plane from the mean equinox of date is computed by

$$\Omega = 125^\circ 02' 40'' 280 - 1934^\circ 08' 10'' 539T + 7'' 455T^2 + 0'' 008T^3, \quad (20)$$

where T is the TDB time in Julian centuries (36,525 days) from J2000.0. The nutation angles in longitude, $\Delta\psi$, and obliquity, $\Delta\varepsilon$, are given by

$$\Delta\psi = -17'' 1996 \sin \Omega, \quad (21)$$

$$\Delta\varepsilon = 9'' 2025 \cos \Omega. \quad (22)$$

The true pole of date unit vector, \mathbf{p}_d , is computed by rotating the Earth-fixed pole vector by the effect of the 18.6 year nutation term to give

$$\mathbf{p}_d = \begin{bmatrix} \sin(\Delta\psi) \sin(\bar{\varepsilon} + \Delta\varepsilon) \\ \cos(\Delta\psi) \sin(\bar{\varepsilon} + \Delta\varepsilon) \cos(\bar{\varepsilon}) - \cos(\bar{\varepsilon} + \Delta\varepsilon) \sin(\bar{\varepsilon}) \\ \cos(\Delta\psi) \sin(\bar{\varepsilon} + \Delta\varepsilon) \sin(\bar{\varepsilon}) + \cos(\bar{\varepsilon} + \Delta\varepsilon) \cos(\bar{\varepsilon}) \end{bmatrix}, \quad (23)$$

where the mean obliquity $\bar{\varepsilon}$ is given by

$$\bar{\varepsilon} = 84381'' 448 - 46'' 815T - 0'' 00059T^2 + 0'' 001813T^3. \quad (24)$$

The pole unit vector in the inertial frame \mathbf{p}_E is computed by precessing the pole of date to inertial coordinates using the long-term precession model (Vondrak et al. 2011) plus an estimated frame offset in x and y rotations,

$$\mathbf{p}_E = \mathcal{R}_V \mathcal{R}_x(-\Phi_x) \mathcal{R}_y(-\Phi_y) \mathbf{p}_d, \quad (25)$$

where Φ_x and Φ_y are the estimated offsets of the EME2000 pole from the ICRF pole and the precession matrix \mathcal{R}_V is given by

$$\mathcal{R}_V = \begin{bmatrix} (\mathbf{n} \times \mathbf{k}) / |\mathbf{n} \times \mathbf{k}| \\ \mathbf{n} \times (\mathbf{n} \times \mathbf{k}) / |\mathbf{n} \times (\mathbf{n} \times \mathbf{k})| \\ \mathbf{n} / |\mathbf{n}| \end{bmatrix}, \quad (26)$$

where \mathbf{k} is the ecliptic pole vector and \mathbf{n} is the mean equatorial pole vector, derived from polynomial fits to a numerically integrated long-term orientation of Earth (Vondrak et al. 2011). The $|\cdot|$ operator represents the norm of a vector.

3. Translational Equations of Motion

This section presents the dynamical models of the planetary and lunar ephemerides, including changes and updates made compared to DE430. Some materials from DE430 (Folkner et al. 2014) are repeated so that this paper can be self-contained and the results can be reproduced.

3.1. Point-mass Acceleration

The point-mass interaction between planetary bodies is governed by the parameterized post-Newtonian (PPN) formulation

Table 2
Planetary Masses Used in DE440 and DE441

Parameter	Value
GM_{Sun}	132712440041.279419 km ³ s ⁻² (estimated from DE440)
GM_{Mercury}	22031.868551 km ³ s ⁻² (Konopliv et al. 2020)
GM_{Venus}	324858.592000 km ³ s ⁻² (Konopliv et al. 1999)
GM_{Earth}	398600.435507 km ³ s ⁻² (estimated from DE440)
$GM_{\text{Mars System}}$	42828.375816 km ³ s ⁻² (Konopliv et al. 2016)
$GM_{\text{Jupiter System}}$	126712764.100000 km ³ s ⁻² (SSD JPL 2020)
$GM_{\text{Saturn System}}$	37940584.841800 km ³ s ⁻² (SSD JPL 2020)
$GM_{\text{Uranus System}}$	5794556.400000 km ³ s ⁻² (Jacobson 2014)
$GM_{\text{Neptune System}}$	6836527.100580 km ³ s ⁻² (Jacobson 2009)
$GM_{\text{Pluto System}}$	975.500000 km ³ s ⁻² (Brozovic et al. 2015)
GM_{Moon}	4902.800118 km ³ s ⁻² (estimated from DE440)
GM_{Ceres}	62.62890 km ³ s ⁻² (Park et al. 2016; Konopliv et al. 2018; Park et al. 2019, 2020a)
GM_{Vesta}	17.288245 km ³ s ⁻² (Konopliv et al. 2014; Park et al. 2014)

(Will & Nordtvedt 1972; Moyer 2003)

$$\begin{aligned} \mathbf{a}_{i,\text{pm-pm}} = & \sum_{j \neq i} \frac{GM_j (\mathbf{r}_j - \mathbf{r}_i)}{r_{ij}^3} \left\{ 1 - \frac{2(\beta + \gamma)}{c^2} \right. \\ & \times \sum_{k \neq i} \frac{GM_k}{r_{ik}} - \frac{2\beta - 1}{c^2} \sum_{k \neq j} \frac{GM_k}{r_{jk}} \\ & + \gamma \left(\frac{v_i}{c} \right)^2 + (1 + \gamma) \left(\frac{v_j}{c} \right)^2 - \frac{2(1 + \gamma)}{c^2} \mathbf{v}_i \cdot \mathbf{v}_j \\ & \left. - \frac{3}{2c^2} \left[\frac{(\mathbf{r}_i - \mathbf{r}_j) \cdot \mathbf{v}_j}{r_{ij}} \right]^2 + \frac{1}{2c^2} (\mathbf{r}_j - \mathbf{r}_i) \cdot \mathbf{a}_j \right\} \\ & + \frac{1}{c^2} \sum_{j \neq i} \frac{GM_j}{r_{ij}^3} \{ [\mathbf{r}_i - \mathbf{r}_j] \cdot [(2 + 2\gamma) \mathbf{v}_i \\ & - (1 + 2\gamma) \mathbf{v}_j] \} (\mathbf{v}_i - \mathbf{v}_j) \\ & + \frac{(3 + 4\gamma)}{2c^2} \sum_{j \neq i} \frac{GM_j \mathbf{a}_j}{r_{ij}}, \end{aligned} \quad (27)$$

where the summations are over all bodies, and β and γ are the Eddington–Robertson–Schiff parameters representing the measure of nonlinearity in the superposition law for gravity and the amount of space curvature produced by a unit rest mass, respectively, and are constrained to unity as predicted by the general theory of relativity (GTR).

DE440 integrated the same set of bodies (i.e., Sun, barycenter of eight planets, the Moon, Pluto barycenter, and 343 asteroids) used in DE430, but also included perturbations from 30 KBOs and a KBO ring discussed in Section 2.2. The key mass parameters used in DE440 are shown in Table 2, and all other relevant parameters are given in the comment blocks of the DE440 and DE441 files.

3.2. Point-mass Interaction with Extended Bodies

Nonspherical gravitational interaction has been modeled using a spherical harmonic expansion. For Earth, the interaction of the zonal harmonics up to the fifth degree and the point masses of the Moon, Sun, Mercury, Venus, Mars, Jupiter, and Saturn have been modeled. For the Moon, the interaction of a

degree and order 6 gravity field and the point masses of Earth, Sun, Mercury, Venus, Mars, Jupiter, and Saturn have been modeled. For the Sun, the interaction of the second-degree zonal harmonic with all other bodies has been modeled.

The acceleration due to an extended body can be represented as

$$\begin{aligned} \begin{bmatrix} \ddot{\xi} \\ \ddot{\eta} \\ \ddot{\zeta} \end{bmatrix} &= -\frac{GM}{r^2} \left\{ \sum_{n=2}^{n_1} J_n \left(\frac{R}{r} \right)^n \begin{bmatrix} (n+1)P_n(\sin \varphi) \\ 0 \\ -\cos \varphi P'_n(\sin \varphi) \end{bmatrix} + \sum_{n=2}^{n_2} \left(\frac{R}{r} \right)^n \right. \\ &\times \left. \sum_{m=1}^n \begin{bmatrix} -(n+1)P_{nm}(\sin \varphi)(+C_{nm} \cos m\lambda + S_{nm} \sin m\lambda) \\ m \sec \varphi P_{nm}(\sin \varphi)(-C_{nm} \sin m\lambda + S_{nm} \cos m\lambda) \\ \cos \varphi P'_{nm}(\sin \varphi)(+C_{nm} \cos m\lambda + S_{nm} \sin m\lambda) \end{bmatrix} \right\}, \end{aligned} \quad (28)$$

where the $\xi\eta\zeta$ coordinate system is defined such that the ξ -axis is defined outward from the extended body to the point mass, the $\xi\zeta$ -plane contains the figure spin-pole of the extended body, and the η -axis completes the triad. Here, r is the distance between the two bodies; n_1 and n_2 represent the maximum degrees of the zonal and nonzonal spherical harmonic coefficients, respectively; P_n and P_{nm} represent the unnormalized degree- n Legendre polynomial and associated Legendre function with degree- n and order- m , respectively; P'_n and P'_{nm} represent the derivative of P_n and P_{nm} with respect to $\sin \varphi$, respectively; J_n represents the degree- n zonal harmonic coefficient; C_{nm} and S_{nm} represent the nonzonal spherical harmonic coefficients for the extended body; R represents the reference radius of the extended body; and λ and φ represent the longitude and latitude of the point mass in the extended-body fixed coordinate system. Once the accelerations are computed in the body fixed frame, they are transformed into the inertial frame for integration.

There is also an interaction between the figure of an extended body and a point mass, often called the indirect acceleration. Given $\mathbf{a}_{i,\text{figi-pmj}}$, which denotes the acceleration of the extended body i interacting with the point-mass external body j expressed in an inertial frame, the corresponding indirect acceleration of the point mass, $\mathbf{a}_{j,\text{figi-pmj}}$, is

$$\mathbf{a}_{j,\text{figi-pmj}} = -\frac{m_i}{m_j} \mathbf{a}_{i,\text{figi-pmj}}. \quad (29)$$

For the Moon, the second-degree spherical harmonic coefficients vary with time due to distortion by tides and rotation. These coefficients are computed from the moment of inertia tensors as a function of time and the detailed description is given in Section 4. The second-degree spherical harmonic coefficients are given by

$$J_{2,M}(t) = \frac{2I_{33,T}(t) - [I_{11,T}(t) + I_{22,T}(t)]}{2m_M R_M^2}, \quad (30)$$

$$C_{22,M}(t) = \frac{I_{22,T}(t) - I_{11,T}(t)}{4m_M R_M^2}, \quad (31)$$

$$C_{21,M}(t) = \frac{-I_{13,T}(t)}{m_M R_M^2}, \quad (32)$$

$$S_{21,M}(t) = \frac{-I_{23,T}(t)}{m_M R_M^2}, \quad (33)$$

$$S_{22,M}(t) = \frac{-I_{12,T}(t)}{2m_M R_M^2}, \quad (34)$$

where $I_{ij,T}$ represent the elements of the total lunar moment of inertia matrix (see Section 4), m_M is the lunar mass, and R_M is the lunar radius.

3.3. Acceleration of the Moon from Earth Tides

The lunar orbit is affected by the tides raised on Earth by the Sun and Moon. The tidal distortion of Earth can be modeled using the second-degree gravitational Love numbers, $k_{2j,E}$, where the order j is 0, 1, and 2 for long-period, diurnal, and semidiurnal responses, respectively. See Section 2.2 in Williams & Boggs (2016) for more information.

A time-delay tidal model has been applied to account for the tidal dissipation. The distorted response of Earth is delayed with respect to the tide-raising forces from the Moon or Sun. The appropriate time delay depends on the period of each tidal component. Consequently, different time delays have been employed for each order j . To allow for time delays shifting across the diurnal and semidiurnal frequency bands, separate time delays are associated with Earth's rotation and the lunar orbit.

The acceleration of the Moon due to the Earth tides is evaluated separately for the tides raised by the Sun and the tides raised by the Moon. The Earth tides depend on the position of the tide-raising body with respect to Earth, \mathbf{r}_T , where T can denote either the Sun or the Moon. The position of the tide-raising body is evaluated at an earlier time $t - \tau'_j$, where τ'_j denotes the orbital time lag, for long-period ($j=0$), diurnal ($j=1$), and semi-diurnal ($j=2$) responses. The rotational distortion of Earth is delayed by a rotational time lag τ_j , so that the distortion leads the direction to the tide-raising body by an angle $\dot{\theta}\tau_j$, where $\dot{\theta}$ is the rotation rate of Earth. The long-period zonal tides ($j=0$) do not depend on the rotation of Earth, so $\tau_j=0$. The acceleration of the Moon due to the distorted Earth depends on the position of the Moon with respect to Earth (\mathbf{r}) and on the modified position vector for the tide-raising body (\mathbf{r}_j^*) that is given for each order j by

$$\mathbf{r}_j^* = \mathcal{R}_E^T \mathcal{R}_z(-\dot{\theta}\tau_j) \mathcal{R}_E \mathbf{r}_T(t - \tau'_j), \quad (35)$$

where \mathcal{R}_E rotates the time-delayed position of the tide-raising body with respect to Earth from the inertial frame to the Earth fixed frame and \mathcal{R}_z here means a right-handed rotation of the vector $\mathbf{r}_T(t - \tau'_j)$ by the angle $-\dot{\theta}\tau_j$ about Earth's rotation axis.

For evaluation of the acceleration of the Moon, the vectors \mathbf{r} (Moon with respect to Earth) and \mathbf{r}_j^* (time-delayed position of a tide-raising body with respect to Earth) are expressed in cylindrical coordinates with the Z-axis perpendicular to Earth's equator so that $\mathbf{r} = \boldsymbol{\rho} + \mathbf{z}$ and $\mathbf{r}_j^* = \boldsymbol{\rho}_j^* + \mathbf{z}_j^*$.

The acceleration of the Moon due to the tide raised on Earth by each tide-raising body (Sun or Moon), $\mathbf{a}_{M,\text{tide}}$ is given by

$$\begin{aligned} \mathbf{a}_{M,\text{tide}} = & \frac{3}{2} \left(\frac{m_E + m_M}{m_E} \right) \frac{Gm_T R_E^5}{r^5} \left\{ \frac{k_{20,E}}{r_1^{*5}} \left([2z_0^{*2} \mathbf{z} + \rho_0^{*2} \boldsymbol{\rho}] \right. \right. \\ & \left. \left. - \frac{5[(zz_0^*)^2 + \frac{1}{2}(\rho\rho_0^*)^2]}{r^2} \mathbf{r} + r_0^{*2} \mathbf{r} \right) \right. \\ & + \frac{k_{21,E}}{r_1^{*5}} \left([2(\boldsymbol{\rho} \cdot \boldsymbol{\rho}_1^*) z_1^* + z z_1^* \boldsymbol{\rho}_1^*] - \frac{10z z_1^* (\boldsymbol{\rho} \cdot \boldsymbol{\rho}_1^*) \mathbf{r}}{r^2} \right) \\ & + \frac{k_{22,E}}{r_2^{*5}} \left([2(\boldsymbol{\rho} \cdot \boldsymbol{\rho}_2^*) \boldsymbol{\rho}_2^* - \rho_2^{*2} \boldsymbol{\rho}] \right. \\ & \left. \left. - \frac{5[(\boldsymbol{\rho} \cdot \boldsymbol{\rho}_2^*)^2 - \frac{1}{2}(\rho\rho_2^*)^2]}{r^2} \mathbf{r} \right) \right\}, \end{aligned} \quad (36)$$

where m_T is the mass of the tide-raising body.

The tidal acceleration due to tidal dissipation is implicit in the above acceleration. Tides raised on Earth by the Moon do not influence the motion of the EMB. The effect of Sun-raised tides on the barycentric motion is not considered.

The tidal bulge leads the Moon and its gravitational attraction accelerates the Moon forward and retards Earth's spin. Energy and angular momentum are transferred from Earth's rotation to the lunar orbit. Consequently, the Moon moves away from Earth, the lunar orbit period lengthens, and Earth's day becomes longer. Some energy is dissipated in Earth rather than being transferred to the orbit.

3.4. LT Acceleration

In DE440, the acceleration of each body other than the Sun due to the gravito-magnetic effect of GTR, also known as the LT effect, has been implemented (Moyer 2003; Park et al. 2017):

$$\mathbf{a}_{i,\text{LT}} = 2\boldsymbol{\Omega}_i \times \mathbf{v}_i, \quad (37)$$

where the LT angular velocity vector $\boldsymbol{\Omega}_i$ is given by

$$\boldsymbol{\Omega}_i = \frac{(1 + \gamma)G}{2c^2 r_i^3} \left[-\mathbf{J} + \frac{3(\mathbf{J} \cdot \mathbf{r}_i) \mathbf{r}_i}{r_i^2} \right], \quad (38)$$

$$\mathbf{J} = C_\odot M_\odot R_\odot^2 \omega_\odot \hat{\mathbf{p}}, \quad (39)$$

where G is the universal gravitational constant, γ is the Eddington–Robertson–Schiff parameter from Section 3.1, c is the speed of light, \mathbf{r}_i is position of the body with respect to the Sun, M_\odot is the Sun's mass, C_\odot is the Sun's polar moment of inertia divided by $(M_\odot R_\odot^2)$, where $C_\odot/(M_\odot R_\odot^2) = 0.06884$, R_\odot is the Sun's equatorial radius (696,000 km), ω_\odot is the Sun's rotation rate (14.1844 deg/day), and $\hat{\mathbf{p}}$ is the unit spin-pole direction of the Sun (R.A. of 286°13 and decl. of 63°87; Archinal et al. 2018).

The LT effect is small, but it is important for fitting the MESSENGER range data (Park et al. 2017). Overall, the LT effect causes Mercury's perihelion to precess at the rate of about $-0''.0020/\text{Julian century}$, which is about 7% of the precession caused by the solar oblateness.

3.5. Solar Radiation Pressure

Photons carry energy and momentum so there is a very small force directed away from the Sun. Like Newtonian gravity, solar radiation pressure depends on the inverse-square distance of the Sun. A simple solar radiation pressure model has been implemented for Earth and the Moon, with accelerations given by

$$\mathbf{a}_{E,\text{srp}} = -\varepsilon_{E,\text{srp}} \frac{GM_{\text{Sun}} \mathbf{r}_{\text{SE}}}{r_{\text{SE}}^3}, \quad (40)$$

$$\mathbf{a}_{M,\text{srp}} = -\varepsilon_{M,\text{srp}} \frac{GM_{\text{Sun}} \mathbf{r}_{\text{SM}}}{r_{\text{SM}}^3}, \quad (41)$$

where the acceleration due to solar radiation pressure is a very small fraction of gravitational acceleration (Vokrouhlický 1997), i.e., $\varepsilon_{E,\text{srp}} = 2 \times 10^{-14}$ for Earth and $\varepsilon_{M,\text{srp}} = 1.44 \times 10^{-13}$ for the Moon. Here, \mathbf{r}_{SE} is the inertial Sun-to-Earth position vector and \mathbf{r}_{SM} is the inertial Sun-to-Moon position vector.

4. Rotational Dynamics of the Moon

The Moon is modeled as an anelastic mantle with a liquid core. The orientations of the core and mantle are numerically integrated for the core and mantle angular velocities. The angular momentum vectors of the mantle and core are the product of the angular velocities and the moments of inertia. The angular momentum vectors change with time due to torques and due to the distortion of the mantle.

4.1. Rate of Change of Lunar Angular Velocities

In a rotating system, the change in angular velocity $\boldsymbol{\omega}$ is related to torques \mathbf{N} by

$$\mathbf{N} = \frac{d}{dt}(\mathbf{I}\boldsymbol{\omega}) + \boldsymbol{\omega} \times \mathbf{I}\boldsymbol{\omega}, \quad (42)$$

where \mathbf{I} is the moment of inertia tensor. The second term on the right-hand side puts the time derivative into the rotating system. The total lunar moment of inertia \mathbf{I}_T , which is the sum of the moment of inertia of the mantle \mathbf{I}_m and the moment of inertia of the core \mathbf{I}_c , is proportional to the mass m_M times the square of the radius R_M . Because the fractional uncertainty in the constant of gravitation G is much larger than that for the lunar mass parameter Gm_M , Equation (42) is evaluated in the integration with both sides multiplied by G .

The components of vectors can be given in the inertial frame, mantle frame, or other frames. Since the moment of inertia matrices are nearly diagonal in the mantle frame, there is great convenience to inverting matrices and performing the matrix multiplications in the mantle frame. The resulting vector components can then be rotated to other frames if desired.

The moment of inertia of the mantle varies with time due to tidal distortions. The distortions are functions of the lunar position and rotational velocities computed at time $t - \tau_m$, where τ_m is a time lag determined from the fits to the LLR data. The time delay allows for dissipation when flexing the Moon. The time derivative of the angular velocity of the mantle is

given by

$$\begin{aligned} \dot{\boldsymbol{\omega}}_m = \mathbf{I}_m^{-1} & \left[\sum_{j \neq M} N_{M, \text{fig}M-\text{pm}j} + N_{M, \text{fig}M-\text{fig}E} - \dot{\mathbf{I}}_m \boldsymbol{\omega}_m \right. \\ & \left. - (\boldsymbol{\omega}_m - \boldsymbol{\nu}_{\text{gp}}) \times \mathbf{I}_m \boldsymbol{\omega}_m + N_{\text{cmb}} \right], \end{aligned} \quad (43)$$

where \mathbf{I}_m is the lunar mantle moment of inertia matrix, $N_{M, \text{fig}M-\text{pm}j}$ is the torque on the lunar mantle due to the point-mass body j , $N_{M, \text{fig}M-\text{fig}E}$ is the torque on the lunar mantle due to the interaction between the extended figure of the Moon and the extended figure of Earth, $\boldsymbol{\nu}_{\text{gp}}$ is the angular rate due to geodetic precession, and N_{cmb} is the torque due to the interaction between lunar mantle and core. The geodetic precession rate is defined as

$$\boldsymbol{\nu}_{\text{gp}} = \mathbf{L} \left[\frac{(1 + 2\gamma)}{2c^2} \mathbf{v}_{\text{EM}} \times \left(\frac{GM_{\text{Earth}} \mathbf{r}_{\text{EM}}}{r_{\text{EM}}^3} + \frac{GM_{\text{Sun}} \mathbf{r}_{\text{SM}}}{r_{\text{SM}}^3} \right) \right], \quad (44)$$

where \mathbf{L} is the rotation matrix from the mean J2000 frame to the lunar body fixed (i.e., selenographic) frame, \mathbf{v}_{EM} is the inertial Earth-to-Moon velocity vector, \mathbf{r}_{EM} is the inertial Earth-to-Moon position vector, and \mathbf{r}_{SM} is the inertial Sun-to-Moon position vector.

The fluid core is assumed to be rotating like a solid and constrained by the shape of the core–mantle boundary at the interior of the mantle, with the moment of inertia constant in the frame of the mantle. The time derivative of the angular velocity of the core expressed in the mantle frame is given by

$$\dot{\boldsymbol{\omega}}_c = \mathbf{I}_c^{-1} [-(\boldsymbol{\omega}_m - \boldsymbol{\nu}_{\text{gp}}) \times \mathbf{I}_c \boldsymbol{\omega}_c - N_{\text{cmb}}], \quad (45)$$

where \mathbf{I}_c is the lunar core moment of inertia matrix.

4.2. Lunar Moments of Inertia

In the mantle frame, the undistorted moment of inertia of the mantle and the moment of inertia of the core are diagonal. The undistorted total moment of inertia $\tilde{\mathbf{I}}_T$ is given by

$$\tilde{\mathbf{I}}_T = \begin{bmatrix} A_T & 0 & 0 \\ 0 & B_T & 0 \\ 0 & 0 & C_T \end{bmatrix}, \quad (46)$$

with A_T , B_T , and C_T given by

$$A_T = \frac{2(1 - \beta_L \gamma_L)}{(2\beta_L - \gamma_L + \beta_L \gamma_L)} m_M R_M^2 \tilde{J}_{2,M}, \quad (47)$$

$$B_T = \frac{2(1 + \gamma_L)}{(2\beta_L - \gamma_L + \beta_L \gamma_L)} m_M R_M^2 \tilde{J}_{2,M}, \quad (48)$$

$$C_T = \frac{2(1 + \beta_L)}{(2\beta_L - \gamma_L + \beta_L \gamma_L)} m_M R_M^2 \tilde{J}_{2,M}, \quad (49)$$

where m_M is the mass of the Moon, R_M is the reference radius of the Moon, $\tilde{J}_{2,M}$ is the second-degree zonal harmonic of the undistorted Moon, and β_L and γ_L are ratios of the undistorted moments of inertia given by

$$\beta_L = \frac{(C_T - A_T)}{B_T}, \quad (50)$$

$$\gamma_L = \frac{(B_T - A_T)}{C_T}. \quad (51)$$

The undistorted total moment of inertia and the second-degree zonal harmonic of the undistorted Moon are not the same as the mean values since the tidal distortions have non-zero averages.

We assume that the lunar rotation aligns an oblate core–mantle boundary with the equator. Then the moment of inertia of the core \mathbf{I}_c is given by

$$\mathbf{I}_c = \alpha_c C_T \begin{bmatrix} 1 - f_c & 0 & 0 \\ 0 & 1 - f_c & 0 \\ 0 & 0 & 1 \end{bmatrix} = \begin{bmatrix} A_c & 0 & 0 \\ 0 & B_c & 0 \\ 0 & 0 & C_c \end{bmatrix}, \quad (52)$$

where $\alpha_c = C_c/C_T$ is the ratio of the core polar moment of inertia to the undistorted total polar moment of inertia and f_c is the core oblateness. Distortion of the core moment of inertia is not considered.

The undistorted moment of inertia of the mantle is the difference between the undistorted total moment of inertia and the core moment of inertia:

$$\tilde{\mathbf{I}}_m = \tilde{\mathbf{I}}_T - \mathbf{I}_c. \quad (53)$$

The moment of inertia of the mantle varies with time due to tidal distortion by Earth and spin distortion, where the position vector of Earth relative to Moon, \mathbf{r} , and the angular velocity of the mantle, $\boldsymbol{\omega}_m$, are evaluated at time

$$\begin{aligned} \mathbf{I}_m(t) = \tilde{\mathbf{I}}_m - \frac{k_{2,M} m_E R_M^5}{r^5} & \begin{bmatrix} x^2 - \frac{1}{3} r^2 & xy & xz \\ xy & y^2 - \frac{1}{3} r^2 & yz \\ xz & yz & z^2 - \frac{1}{3} r^2 \end{bmatrix} \\ + \frac{k_{2,M} R_M^5}{3G} & \begin{bmatrix} \omega_{m,x}^2 - \frac{1}{3} (\omega_m^2 - n^2) & \omega_{m,x} \omega_{m,y} & \omega_{m,x} \omega_{m,z} \\ \omega_{m,x} \omega_{m,y} & \omega_{m,y}^2 - \frac{1}{3} (\omega_m^2 - n^2) & \omega_{m,y} \omega_{m,z} \\ \omega_{m,x} \omega_{m,z} & \omega_{m,y} \omega_{m,z} & \omega_{m,z}^2 - \frac{1}{3} (\omega_m^2 + 2n^2) \end{bmatrix}, \end{aligned} \quad (54)$$

Table 3
Observational Data for the Moon and Inner Planets

Body	Classification	Type	Observatory/Spacecraft	Span	Number		
Moon	LLR	Range	McDonald 2.7 m	1970–1986	3440		
			MLRS/saddle	1985–1989	275		
			MRLS/Mt Fowlkes	1988–2014	2870		
			Haleakala	1984–1991	694		
			Observatoire de la Côte d’Azur	1984–2020	16425		
			Matera	2003–2020	248		
			Apache Point	2006–2017	2452		
Mercury	Spacecraft	Range	Mariner 10	1974–1975	2		
			MESSENGER	2011–2016	1353		
Venus	Spacecraft	3D	MESSENGER	2008–2010	3		
			Spacecraft	Range	Venus Express	2006–2014	2158
Venus	Spacecraft	3D	Cassini	1998–2000	2		
			Spacecraft	VLBI	MAGELLAN	1990–1995	18
					Venus Express	2007–2015	64
Mars	Spacecraft	Range	Viking Lander 1	1976–1983	1174		
			Viking Lander 2	1976–1978	80		
			Mars Pathfinder	1997	90		
			Mars Express	2005–2020	8751		
			Mars Global Surveyor	1999–2007	2130		
			Mars Odyssey	2002–2020	10087		
			Mars Reconnaissance Orbiter	2006–2020	2634		
	Spacecraft	VLBI	Mars Global Surveyor	2001–2004	15		
			Mars Odyssey	2002–2020	169		
			Mars Reconnaissance Orbiter	2006–2020	123		
	Spacecraft	VLBA	Various	2008–2014	9		

$t - \tau_m$; $k_{2,M}$ is the lunar potential Love number; m_E is the mass of Earth; R_M is the reference radius of the Moon; r is the Earth–Moon distance; x , y , and z are the components of the position of Earth relative to the Moon referred to the mantle frame; $\omega_{m,x}$,

$\omega_{m,y}$, $\omega_{m,z}$ are the components of ω_m in the mantle frame; and n is the lunar mean motion.

The rate of change of the mantle’s moment of inertia is given by

$$\begin{aligned}
\dot{\mathbf{I}}_m = & \frac{5k_{2,M}m_ER_M^5}{r^7} \mathbf{r} \cdot \dot{\mathbf{r}} \begin{bmatrix} x^2 - \frac{1}{3}r^2 & xy & xz \\ xy & y^2 - \frac{1}{3}r^2 & yz \\ xz & yz & z^2 - \frac{1}{3}r^2 \end{bmatrix} \\
& - \frac{k_{2,M}m_ER_M^5}{r^5} \begin{bmatrix} 2\left(x\dot{x} - \frac{1}{3}\mathbf{r} \cdot \dot{\mathbf{r}}\right) & xy + \dot{x}y & x\dot{z} + \dot{x}z \\ xy + \dot{x}y & \left(y\dot{y} - \frac{1}{3}\mathbf{r} \cdot \dot{\mathbf{r}}\right) & y\dot{z} + \dot{y}z \\ x\dot{z} + \dot{x}z & y\dot{z} + \dot{y}z & 2\left(z\dot{z} - \frac{1}{3}\mathbf{r} \cdot \dot{\mathbf{r}}\right) \end{bmatrix} \\
& + \frac{k_{2,M}R_M^5}{3G} \begin{bmatrix} 2\left(\omega_{m,x}\dot{\omega}_{m,x} - \frac{1}{3}\boldsymbol{\omega}_m \cdot \dot{\boldsymbol{\omega}}_m\right) & \omega_{m,x}\dot{\omega}_{m,y} + \dot{\omega}_{m,x}\omega_{m,y} & \omega_{m,x}\dot{\omega}_{m,z} + \dot{\omega}_{m,x}\omega_{m,z} \\ \omega_{m,x}\dot{\omega}_{m,y} + \dot{\omega}_{m,x}\omega_{m,y} & 2\left(\omega_{m,y}\dot{\omega}_{m,y} - \frac{1}{3}\boldsymbol{\omega}_m \cdot \dot{\boldsymbol{\omega}}_m\right) & \omega_{m,y}\dot{\omega}_{m,z} + \dot{\omega}_{m,y}\omega_{m,z} \\ \omega_{m,x}\dot{\omega}_{m,z} + \dot{\omega}_{m,x}\omega_{m,z} & \omega_{m,y}\dot{\omega}_{m,z} + \dot{\omega}_{m,y}\omega_{m,z} & 2\left(\omega_{m,z}\dot{\omega}_{m,z} - \frac{1}{3}\boldsymbol{\omega}_m \cdot \dot{\boldsymbol{\omega}}_m\right) \end{bmatrix}. \quad (55)
\end{aligned}$$

4.3. Lunar Torques

The torque on the Moon due to an external point-mass A is given by

$$\mathbf{N}_{M,\text{fig}M-\text{pm}A} = M_M \mathbf{r}_{AM} \times \mathbf{a}_{M,\text{fig}M-\text{pm}A}, \quad (56)$$

where \mathbf{r}_{AM} is the position of the point mass relative to the Moon and $\mathbf{a}_{M,\text{fig}M-\text{pm}A}$ is the acceleration of the Moon due to the interaction of the extended figure of the Moon with the point-mass A , as described in Section 3.2. Torques are computed for the figure of the Moon interacting with Earth, the Sun, Mercury, Venus, Mars, Jupiter, and Saturn.

It can be shown that torques due to the interaction of the figure of the Moon with the figure of Earth are important for the orientation of the Moon (Eckhardt 1981). The three most significant terms of the torque are

$$\begin{aligned} \mathbf{N}_{M,\text{fig}M-\text{fig}E} = & \frac{15GM_E R_E^2 J_{2,E}}{2r_{EM}^5} \{ (1 - 7 \sin^2 \varphi_{M,E}) \\ & \times [\hat{\mathbf{r}}_{EM} \times \mathbf{I}_M \hat{\mathbf{r}}_{EM}] \\ & + 2 \sin \varphi_{M,E} [\hat{\mathbf{r}}_{EM} \times \mathbf{I}_M \hat{\mathbf{p}}_E + \hat{\mathbf{p}}_E \times \mathbf{I}_M \hat{\mathbf{r}}_{EM}] \\ & - \frac{2}{5} [\hat{\mathbf{p}}_E \times \mathbf{I}_M \hat{\mathbf{p}}_E], \end{aligned} \quad (57)$$

where $\hat{\mathbf{p}}_E$ is the direction vector of Earth's pole and $\hat{\mathbf{r}}_{EM}$ is the direction vector of Earth from the Moon, \mathbf{I}_M is the lunar moment of inertia tensor, R_E is the reference radius of Earth, and $\varphi_{M,E}$ is defined by $\sin \varphi_{M,E} = \hat{\mathbf{r}}_{EM} \cdot \hat{\mathbf{p}}_E$.

The torque on the mantle due to the interaction between the core and mantle is evaluated in the mantle frame and is given by

$$\mathbf{N}_{\text{cmb}} = k_v (\boldsymbol{\omega}_c - \boldsymbol{\omega}_m) + (C_c - A_c) (\hat{\mathbf{z}}_m \cdot \boldsymbol{\omega}_m) (\hat{\mathbf{z}}_m \times \boldsymbol{\omega}_c), \quad (58)$$

where $\hat{\mathbf{z}}_m$ is a unit vector in the mantle frame aligned with the polar axis. Parameter k_v is for the viscous interaction at the core–mantle boundary. The torque on the core is the negative of the torque on the mantle.

5. Observational Data Used for Computing DE440 and DE441

The observations that have been used to compute DE440 and DE441 are summarized in Tables 3–5 for each body.

An LLR observation measures the round-trip light time from an LLR station on Earth to a retroreflector on the Moon. There are five retroreflectors on the Moon: the Apollo 11, 14, and 15 landing sites and the Lunokhod 2 and 1 rovers. The LLR measurements started in 1970 following the first landings of astronauts and continue to the present. The LLR residuals can be expressed as one-way range residuals, i.e., one-way residual $= \frac{(t_{\text{measured}} - t_{\text{computed}})c}{2}$. The LLR measurement accuracy has improved with time as technology for producing short-duration high-energy laser pulses and timing measurements has advanced.

Spacecraft measurements are based on the Deep Space Network (DSN) radio range, Doppler, and VLBI measurements. For spacecraft in orbit about the planet, the Doppler measurements are typically used to estimate the position of the spacecraft with respect to the planet's center of mass and then range and VLBI measurements are used to estimate the orbit of the planet. For spacecraft flying by a planet, the range, Doppler,

Table 4
Observational Data for Jupiter, Saturn, and Uranus

Body	Classification	Type	Observatory/ Spacecraft	Span	Number
Jupiter	Spacecraft	Range	Juno	2016–2020	15
	Spacecraft	3D	Pioneer 10	1973	1
			Pioneer 11	1974	1
			Voyager 1	1979	1
			Voyager 2	1979	1
			Ulysses	1992	1
			Cassini	2000	1
			New Horizons	2007	1
	Spacecraft	VLBA	Juno	2016–2019	6
	Spacecraft	VLBI	Galileo	1996–1998	22
Saturn	Spacecraft	Range	Cassini	2004–2018	147
	Spacecraft	VLBA	Cassini	2004–2018	27
	Spacecraft	3D	Voyager 1	1980	1
			Voyager 2	1981	1
	Astrometric	CCD	Flagstaff	1998–2016	3152
			Table Mountain	2001–2010	687
			Nikolaev	1973–1998	588
	Astrometric	Relative	Yerkes	1910–1922	18
Uranus	Spacecraft	3D	Voyager 2	1986	1
	Astrometric	CCD	Flagstaff	1995–2016	2362
			Table Mountain	1998–2010	324
			Nikolaev	1961–1999	215
	Astrometric	Relative	Yunnan	2014–2017	3332
			Yerkes	1908–1923	21
	Astrometric	Transit	Bordeaux	1985–1993	165
			La Palma	1984–1997	1030
			Tokyo	1986–1989	44
Washington			1926–1993	1783	

and VLBI data, as available, are used to estimate both the trajectory of the spacecraft and a 3D position of the planet, given as range, R.A., and decl.

Range measurements to spacecraft are usually made at regular intervals during a tracking pass, typically every 10 minutes, while Doppler measurements are made more frequently, typically every minute. Both range and Doppler measurements are based on the measurement of the phase of a radio signal, with the carrier signal used for Doppler and a ranging modulation signal used for range. Since the carrier signal is at a much higher frequency and usually has much higher signal strength, Doppler measurements change in range much more accurately than the range measurements. Because of the shorter wavelength associated with the higher frequency, the integer number of carrier wavelengths cannot be resolved, so Doppler measurements do not allow for an estimation of absolute range. Range measurements are more accurate measurements of round-trip light time. For plotting residuals, one-way residuals are used, which are essentially the same as the LLR residuals, i.e., one-way range $= \frac{(t_{\text{measured}} - t_{\text{computed}})c}{2}$. The range measurement accuracy is often limited by a calibration of the signal path delay in the tracking station prior to each tracking pass. Since this calibration error is common to all range measurements in the tracking pass, there is only one

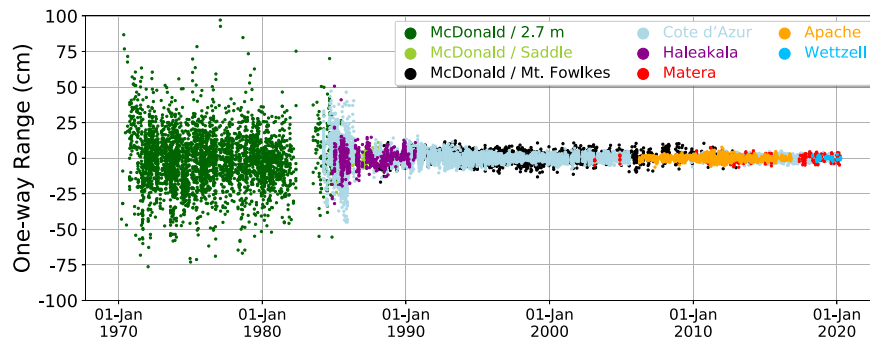


Figure 4. Residuals of LLR ranges against DE440. The rms residual of the LLR ranges is about 20 cm for the early data and is about 1.3 cm for the recent data.

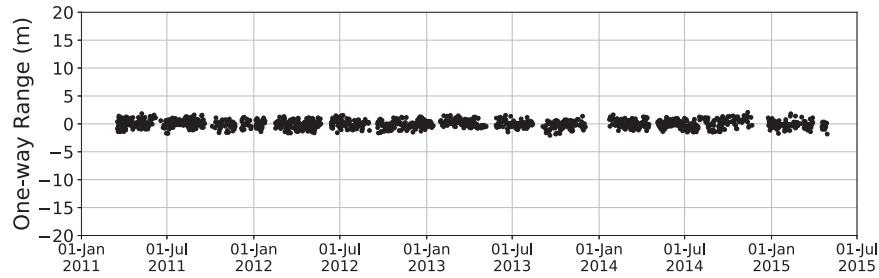


Figure 5. Residuals of the MESSENGER range data against DE440. The rms residual of the MESSENGER ranges is about 0.7 m.

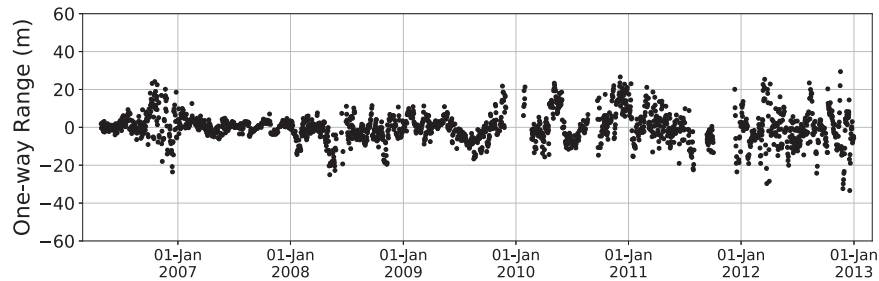


Figure 6. Residuals of the Venus Express range data against DE440. The rms residual of the Venus Express ranges is about 8 m.

Table 5
Observational Data for Neptune and Pluto

Body	Classification	Type	Observatory/Spacecraft	Span	Number
Neptune	Spacecraft	3D	Voyager 2	1989	1
	Astrometric	CCD	Flagstaff	1995–2015	2469
			Table Mountain	1998–2013	416
			Nikolaev	1961–1999	218
			Yunnan	2014–2017	755
	Astrometric	Relative	Yerkes	1904–1923	27
	Astrometric	Transit	Bordeaux	1985–1993	183
			La Palma	1984–1998	1106
			Washington	1926–1993	1537
Pluto	Astrometric	Occultation	Various	1988–2017	23
	Astrometric	CCD	Flagstaff	1995–2015	1098
			Table Mountain	2001–2015	549
			Pico dos Dias	1995–2012	5489
	Astrometric	Photographic	Pulkovo	1930–1992	53

statistically independent range point per pass. Therefore, only one range point per tracking pass was used in the data reduction, and the number of range measurements per spacecraft in Tables 3–5 reflect this.

Spacecraft VLBI measurements are usually made using two widely separated tracking stations. The measurements are made using a modulation on the carrier signal (delta-differential one-way range) and give one component of the direction to the

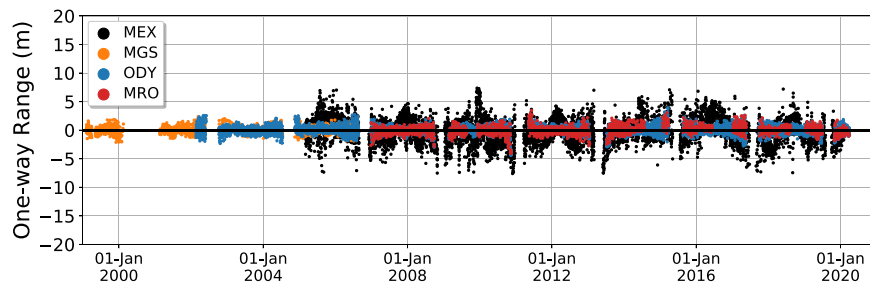


Figure 7. Residuals of the Mars orbiter range data against DE440. The rms residual of the MEX ranges is about 2 m and the rms residuals of the MGS, ODY, and MRO ranges are about 0.7 m.

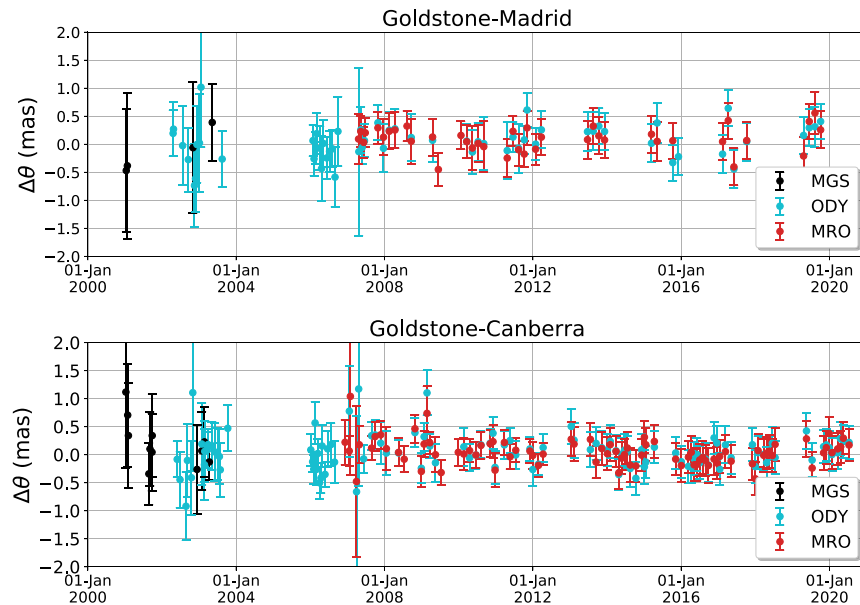


Figure 8. Residuals of Mars orbiter VLBI data against DE440, showing the Goldstone–Madrid baseline (top) and the Goldstone–Canberra baseline (bottom). The rms residual of the Goldstone–Madrid baseline is about 0.25 mas and the rms residual of the Goldstone–Canberra baseline is about 0.18 mas.

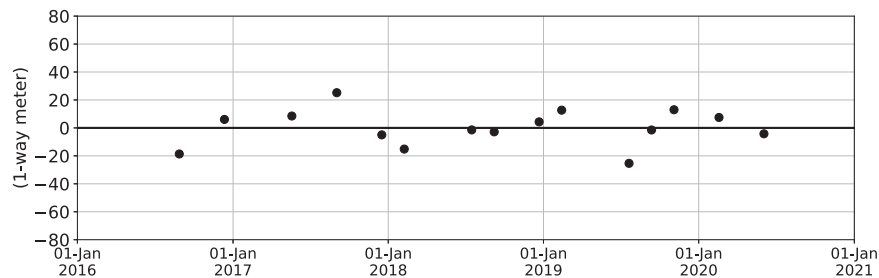


Figure 9. Residuals of the Juno range data against DE440. The rms residual of the Juno ranges is about 13 m.

spacecraft (Thornton & Border 2003). The angular component direction depends on the baseline used. The baseline from Goldstone, California to Madrid, Spain is nearly parallel to Earth’s equator, so measurements on that baseline measure an angular component that is close to the R.A.. The baseline from Goldstone, California to Canberra, Australia has an angle of about 45 degrees relative to the equator, thus, it measures an angular component that is approximately mid-way between the R.A. and decl. directions. Residuals for single-baseline measurements are given for each baseline. For Cassini and Juno (and a few points for Mars orbiters), VLBA was used, where the difference in the time of arrival of the spacecraft carrier signal was used to determine both components of the direction to the spacecraft.

Astrometric measurements record the direction to the planet, namely, R.A. and decl., based on imaging relative to a star field. The accuracy of the star catalog is often the largest source of measurement error. The CCD type indicates more modern observations using electronic detectors, generally referred to star catalogs based on the Hipparcos mission launched in 1991 that are referred to the ICRF2 through the estimation of the positions of radio stars using VLBI. Older measurements were taken using photographic plates or transit methods, often referred to older star catalogs, though corrected to the Hipparcos catalog in some fashion. Barnard measured the angular separation between the outer planets and some of their satellites relative to angularly nearby stars at Yerkes Observatory. The positions of those stars are taken from modern star

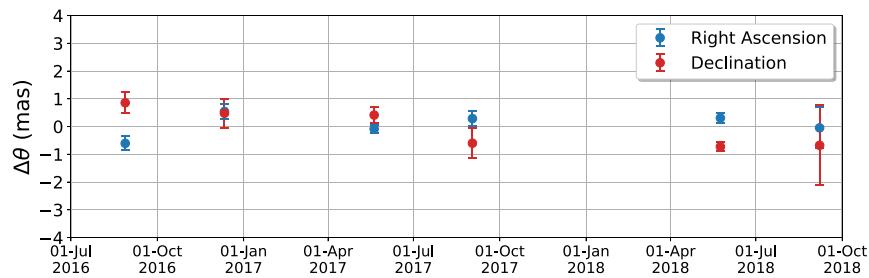


Figure 10. Residuals of the Juno VLBA data against DE440. The rms residual of the Juno VLBA data in R.A. is about 0.4 mas and the rms residual of the Juno VLBA data in decl. is about 0.6 mas.

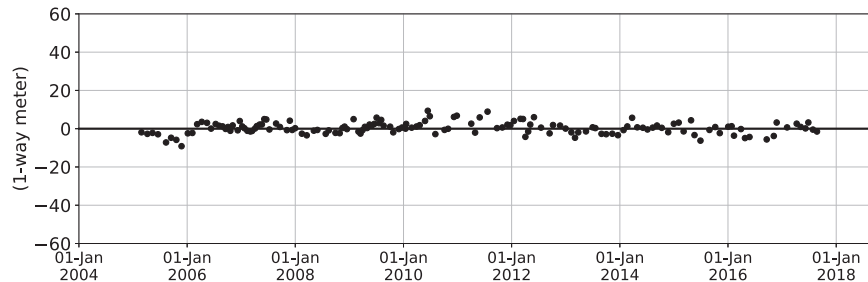


Figure 11. Residuals of the Cassini range data against DE440. The rms residual of the Cassini ranges is about 3 m.

catalogs, with accuracies limited by the knowledge of stellar proper motion. Transit observations cover a longer time span than the more modern spacecraft and astrometric measurements. Since the measurement noise is relatively large for the transit measurements, they do not contribute significantly to the ephemeris solution. The transit measurements are included mainly for historical comparison.

Occultation measurements of Pluto are included here, where the R.A. and decl. are determined from the timed disappearance and reappearance of a star occulted by Pluto (Desmars et al. 2019).

5.1. Residuals

The orbit of the Moon is determined from the LLR data, and Figure 4 shows the one-way residuals of the LLR data over about 50 years. In the last few years, data were available from the Observatoire de la Côte d’Azur, Apache Point, Matera, and Wettzell sites. The rms residual of the early LLR data (~ 1970 – 1980) is about 20 cm while the rms residual of the recent LLR data is about 1.3 cm.

The orbit of Mercury is mainly determined from the MESSENGER radio range data, and Figure 5 shows the one-way range residuals over about 4 years. The rms residual of the MESSENGER ranges is about 0.7 m.

The orbit of Venus is mainly determined from the Venus Express radio range data, and Figure 6 shows the one-way range residuals over about 6.5 years. The rms residual of the Venus Express ranges is about 8 m.

The shape of Mars’ orbit is mainly constrained by the radio range data of Mars orbiters, and Figure 7 shows the one-way range residuals of Mars Express (MEX), Mars Global Surveyor (MGS), Mars Odyssey (ODY), and Mars Reconnaissance Orbiter (MRO). The rms residual of the MEX ranges is about 2 m and the rms residuals of the MGS, ODY, and MRO ranges

are about 0.7 m. The orientation of Mars’ orbit is mainly constrained by VLBI measurements of the Mars orbiters, and Figure 8 shows the VLBI residuals of the Goldstone–Madrid and Goldstone–Canberra baselines. The rms residual of the Goldstone–Madrid baseline is about 0.25 mas and the rms residual of the Goldstone–Canberra baseline is about 0.18 mas.

The shape of Jupiter’s orbit is mainly constrained by the Juno radio range data, and Figure 9 shows the one-way range residuals over about 4 years. The rms residual of the Juno ranges is about 13 m. The orientation of Jupiter’s orbit is mainly constrained by the VLBA data of the Juno spacecraft, and Figure 10 shows the Juno VLBA residuals over about 2 years. The rms residual of the Juno VLBA data in R.A. is about 0.4 mas and the rms residual of the Juno VLBA data in decl. is about 0.6 mas.

The shape of Saturn’s orbit is mainly constrained by the Cassini radio range data, and Figure 11 shows the one-way range residuals over about 13 years. The rms residual of the Cassini ranges is about 3 m. The orientation of Saturn’s orbit is mainly constrained by the VLBA data of the Cassini spacecraft, and Figure 12 shows the Cassini VLBA residuals over about 13 years. The rms residual of the Cassini VLBA data in R.A. is about 0.6 mas and the rms residual of the Cassini VLBA data in decl. is about 0.8 mas if the two obvious outliers are included, and 0.35 and 0.36 mas if they are excluded.

The orbits of Uranus and Neptune are mainly constrained by astrometry and radio range measurements to the Voyager flybys and they are statistically consistent with DE430 (see Folkner et al. 2014).

The orbit of Pluto is mainly determined by astrometry, and Figure 13 shows the residuals of the stellar occultation measurements from Desmars et al. (2019). The rms residuals of the stellar occultations are about 8 mas in R.A. and about 11 mas in decl.

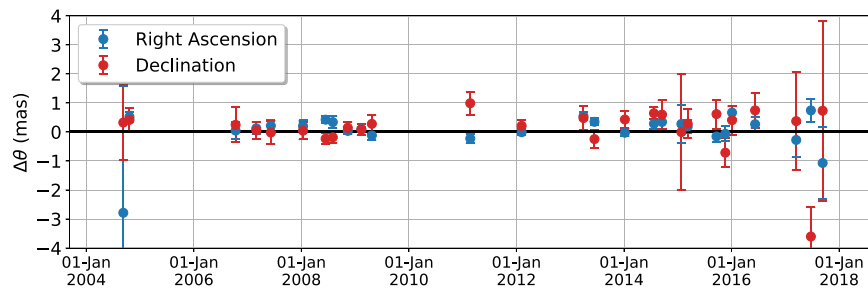


Figure 12. Residuals of the Cassini VLBA data against DE440. The rms residual of the Cassini VLBA data in R.A. is about 0.6 mas and the rms residual of the Cassini VLBA data in decl. is about 0.8 mas if the two obvious outliers are included, and 0.35 and 0.36 mas if they are excluded.

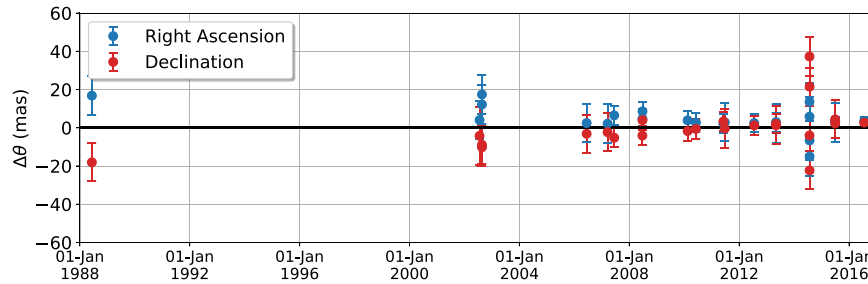


Figure 13. Residuals of stellar occultations of Pluto against DE440. The rms residuals of the stellar occultations are about 8 mas in R.A. and about 11 mas in decl.

6. Conclusions

This paper presents JPL’s new general-purpose ephemerides DE440 and DE441 created by fitting numerically integrated orbits to ground-based and space-based observations. Compared to DE430, the previous general-purpose ephemerides released in 2014, new data spanning over about 7 years have been added to compute DE440. The shapes of the orbits of Mercury, Venus, and Mars are constrained mainly by the radio range data of the MESSENGER, Venus Express, and Mars-orbiting spacecraft, respectively. The orientations of inner planet orbits are tied through the ICRF via VLBI of Mars-orbiting spacecraft. The orbit of the Moon is primarily determined by laser ranging to lunar retroreflectors with the data arc extended through 2020 March. The orbit accuracy of Jupiter has improved substantially by fitting the orbit to the new Juno radio ranges and VLBA data. The orbit of Saturn is determined by radio ranges and VLBA data of the Cassini spacecraft, with improved calibration of the radio range data. The orbits of Uranus and Neptune are constrained by astrometry and radio range measurements to the Voyager flybys. The orbit of Pluto is constrained by stellar occultation data reduced against the Gaia star catalog. DE440 spans years 1550–2650 and DE441 spans years $-13,200$ to $+17,191$. The ephemerides of DE440 are recommended for analyzing modern data while DE441 is recommended for analyzing historic data before the DE440 time span.

The authors would like to thank A. Konopliv, R. Jacobson, J. Border, D. Jones, T. Morely, and F Budnik for providing some of the data used to compute DE440 and DE441. This research was carried out at the Jet Propulsion Laboratory, California Institute of Technology, under a contract with the National Aeronautics and Space Administration. Government sponsorship is acknowledged.

ORCID iDs

Ryan S. Park <https://orcid.org/0000-0001-9896-4585>
 William M. Folkner <https://orcid.org/0000-0001-5133-9934>
 James G. Williams <https://orcid.org/0000-0002-8441-5937>

References

- Almanac, U.S. Nautical Almanac Office & Her Majesty’s Nautical Almanac Office 2018, *The Astronomical Almanac for 2019* (Washington, DC: US Government Printing Office)
- Archinal, B. A., Acton, C. H., A’Hearn, M. F., et al. 2018, *CeMDA*, **130**, 22
- Bolton, S., Levin, S., & Bagenal, F. 2017, *GeoRL*, **44**, 7663
- Brozovic, M., Showalter, M. R., Jacobson, R. A., & Buie, M. W. 2015, *Icar*, **246**, 317
- Charlot, P., Jacobs, C. S., Gordon, D., et al. 2020, *A&A*, **644**, A159
- Desmars, J., Meza, E., Sicardy, B., et al. 2019, *A&A*, **625**, A43
- Eckhardt, D. H. 1981, *M&P*, **25**, 3
- Estabrook, F. B. 1971, Derivation of Relativistic Lagrangian for n-body Equations Containing Relativity Parameters β and γ . JPL Interoffice Memorandum Section 328
- Fienga, A., Avdellidou, C., & Hanus, J. 2020, *MNRAS*, **492**, 589
- Folkner, W. M., & Border, J. S. 2015, *HiA*, **16**, 219
- Folkner, W. M., Williams, J. G., Boggs, D. H., Park, R. S., & Kuchynka, P. 2014, *The Planetary and Lunar Ephemerides DE430 and DE43, IPN Progress Report*, 42-196, https://ipnpr.jpl.nasa.gov/progress_report/42-196/196C.pdf
- Gaia Collaboration, Brown, A. G. A., Vallenari, A., et al. 2018, *A&A*, **616**, A1
- Jacobson, R. A. 2009, *AJ*, **137**, 4322
- Jacobson, R. A. 2014, *AJ*, **148**, 76
- Jones, D. L., Folkner, W. M., Jacobson, R. A., et al. 2020, *AJ*, **159**, 72
- Konopliv, A. S., Asmar, S. W., Park, R. S., et al. 2014, *Icar*, **240**, 103
- Konopliv, A. S., Banerdt, W. B., & Sjogren, W. L. 1999, *Icar*, **139**, 3
- Konopliv, A. S., Park, R. S., & Ermakov, A. I. 2020, *Icar*, **335**, 113386
- Konopliv, A. S., Park, R. S., & Folkner, W. M. 2016, *Icar*, **274**, 253
- Konopliv, A. S., Park, R. S., Vaughan, A. T., et al. 2018, *Icar*, **299**, 411
- Konopliv, A. S., Park, R. S., Yuan, D.-N., et al. 2013, *JGRE*, **118**, 1415
- Lemoine, F. G., Goossens, S., Sabaka, T. J., et al. 2013, *JGRE*, **118**, 1676
- Lieske, J. H. 1979, *A&A*, **73**, 282
- Moyer, T. D. 2003, *Formulation for Observed and Computed Values of Deep Space Network Data Types for Navigation* (Hoboken, NJ: Wiley-Interscience)
- Park, R. S., Folkner, W. M., Jones, D. L., et al. 2015, *AJ*, **150**, 121

- Park, R. S., Folkner, W. M., Konopliv, A. S., et al. 2017, *AJ*, **153**, 121
- Park, R. S., Konopliv, A. S., Asmar, S. W., et al. 2014, *Icar*, **240**, 118
- Park, R. S., Konopliv, A. S., Bills, B. G., et al. 2016, *Natur*, **537**, 515
- Park, R. S., Konopliv, A. S., Ermakov, A. I., et al. 2020a, *NatAs*, **4**, 748
- Park, R. S., Riedel, J. E., Ermakov, A. I., et al. 2020b, *P&SS*, **194**, 105095
- Park, R. S., Vaughan, A. T., Konopliv, A. S., et al. 2019, *Icar*, **319**, 812
- Petit, G., & Luzum, B. 2009, IERS Conventions, IERS Technical Note, 36, <https://www.iers.org/IERS/EN/Publications/TechnicalNotes/tn36.html>
- Pitjeva, E. V., & Pitjev, N. P. 2018, *CeMDA*, **130**, 57
- Rambaux, N., & Williams, J. G. 2011, *CeMDA*, **109**, 85
- Soffel, M., Klioner, S. A., Petit, G., et al. 2003, *AJ*, **126**, 2687
- SSD JPL 2020, JPL Solar System Dynamics, <https://ssd.jpl.nasa.gov>
- Thornton, C. L., & Border, J. S. 2003, Radiometric Tracking Techniques for Deep-space Navigation (Hoboken, NJ: Wiley-Interscience)
- Vallisneri, M., Taylor, S. R., Simon, J., et al. 2020, *ApJ*, **893**, 112
- Vokrouhlický, D. 1997, *Icar*, **126**, 293
- Vondrak, J., Capitaine, N., & Wallace, P. 2011, *A&A*, **534**, A22
- Vondrak, J., Capitaine, N., & Wallace, P. T. 2009, in Proceedings Journées 2008: Systèmes de référence spatio-temporels, ed. M. Soffel & N. Capitaine (Paris: Observatoire de Paris), 23
- Will, C. M., & Nordtvedt, K. 1972, *ApJ*, **177**, 757
- Williams, J. G., & Boggs, D. H. 2016, *CeMDA*, **126**, 89